Numerical and experimental study of micro-convex dimple developed by laser additive manufacturing for surface applications

Vijay Mandal*, Vikas Tiwari, Moloy Sarkar, Sudhanshu S. Singh, J. Ramkumar

Indian Institute of Technology Kanpur, India

Presented in International Conference on Precision, Micro, Meso and Nano Engineering (COPEN - 12: 2022) December 8th - 10th, 2022 IIT Kanpur, India

ABSTRACT

Surface texturing using laser is one such technique exhaustively used for enhancing the surface properties of the components. In this work, a 2D FEM is built to simulate the thermo-fluidic phenomena of surface texturing in the preplaced IN718 powder. Transient heat transfer and fluid flow were used to predict the temperature and velocity fields. Experiments are conducted to develop micro-convex dimple texture on the surface, which usually enhances the surface hydrophobicity and tribological properties. The experimental and numerical results are in good agreement and reveal that with increase in the number of pulses, the height of the micro-convex dimples decreases.

KEYWORDS

Additive Manufacturing,
Convex Dimple,
Texture,
Simulation,
Melt Pool Oscillations.

1. Introduction

Numerous existing texturing fabrication techniques are currently being used in various applications in surface engineering. In present decade, surface texturing has become an essential tool for enhancing surface properties of the components in the field of aerospace, medical and different industrial applications made by different techniques. Lasers have become one of the most useful and accurate tools for surface engineering. This is due to lasers having large temperature gradients and cooling rate (Etsion, 2005; Mandal et al., 2022; Sharma et al., 2019).

In SLM, the different laser scanning patterns induce protuberances on the surface. The surface texture is induced by the induced surface irregularity. For instance, (Simonelli et al., 2014) scan the entire area with parallel scan direction. The scan rotation was changed by 67° for each new layer. It was reported that crystallographic texture formed in three orthogonal planes. (Dinda et al., 2012; Wei et al., 2015) scan the laser beam in forward and backward directions, observing that in unidirectional, a fibre texture is formed, while in bi-directional, a cube texture is formed. The texture on the surface is also induced by insufficient laser beam intensity, spatter formation during scanning, and a partially melted particle on the surface that is loosely associated with the surface. A large number of partially or moderately melted powder particles on the surface induces hydrophobicity with an average contact angle of 102° (Jiao et al., 2018; Sarker et al., 2018). Another way to develop texture on a 3D component is to generate a micro size feature on the surface. The surface micro-feature is intended to improve drag and surface interaction with viscous fluids. The various alternative geometry and orientation have been accomplished with fine micro features. The microfeature, i.e., track width and depth of less than 50 µm size, was achieved (Otero et al., 2012; Wang et al., 2016). Furthermore, texture surfaces were generated by varying hatch space and scanning strategy. Experiment results show that increasing the hatch space surface morphological roughness increases (Romero et al., 2011). As previously discussed, a series of articles on surface texturing using additive manufacturing techniques have been published. However, only a few numerical model articles have been presented, and only the thermal field has been studied during texturing by additive technique (Zhou et al., 2015). A 2D model was developed to examine the thermal and fluid flow dynamics in the melt pool. In this research, a thermo-fluidic mechanism, heating and solidification, was discussed and validated using experimental results. In addition, roles of driving forces i.e., Marangoni force, thermal buoyancy force, recoil pressure,

*Corresponding author E-mail: vijaym@iitk.ac.in

https://doi.org/10.58368/MTT.22.1.2023.45-50

and evaporation have all been investigated. In this study, the experimental results (i.e., optical profilometry images) shows good agreement with the numerical model.

2. Numerical Simulation

To understand the melt pool contour and solidification behavior, a numerical model has been established in COMSOL Multiphysics under the following assumptions:

1. The liquid metal flow in the melt pool is assumed to be laminar, Newtonian and incompressible.
2. The properties of the material are homogenous and isotropic. The thermo-physical properties of IN718 depend on temperature in solidus and liquidus phases.
3. The multiple reflections in the powder bed are not considered in this model.
4. The powder distribution in a given dimension on the top surface of the substrate material is placed manually, and powder size having 25 µm diameter.
5. The atmospheric air is treated as non-reactive.

2.1. Governing equations

The transport phenomena in solid, liquid, and gaseous regions are evaluated simultaneously using mass conservation, momentum conservation, and energy conservation equations [2].

$$\frac{\partial(\rho\vec{u})}{\partial t} + \nabla\cdot(\rho\vec{u}) = 0 \quad \text{.....(1)}$$

$$\frac{\partial(\rho\vec{u})}{\partial t} + \vec{u}.\nabla(\rho\vec{u}) = \nabla\cdot\left[-pI + \mu(\overrightarrow{\nabla u}) + (\overrightarrow{\nabla u})^T\right] - \rho\left(1-\beta(T-T_m)\right)\vec{g} + \vec{F} \quad \text{.....(2)}$$

$$\frac{\partial(\rho C_p T)}{\partial t} + \nabla.(\rho\vec{u}C_p T) = \vec{\nabla}\cdot\left(k\vec{\nabla}T\right) + Q \quad \text{.....(3)}$$

$$F = -C\frac{(1-f_l)^2}{(f_l^3+b)}\vec{u} \quad \text{.....(4)}$$

$$f_l = \begin{cases} 0 & T \le T_s \\ \frac{T-T_s}{T_l-T_s} & T_s \le T \le T_l \\ 1 & T > T_l \end{cases} \quad \text{.....(5)}$$

Where, ρ, $\vec{u}$, C_p, µ, k, β, T_m, g and T are listed in the table 2, and I is the identity matrix, P is pressure (Pa), F is the Darcy damping force, and Q is the net available heat for melting. Equations (4-5) evaluated from Kozeny-Carman equation, which is treated as porous media i.e., mushy zone. In equation 4, the term C is the morphology constant, which has a large value, i.e., 2 × 10^7 (Gan et al., 2017). Another constant term b is a small value, i.e., 10^{-5}, in order to avoid the term $\vec{F}$ to be infinity.

The gas liquid interface is defined by (Mandal et al., 2023)

$$\delta = 6|\phi(1-\phi)|\,|\nabla\phi| \quad \text{.....(6)}$$

The heat flux boundary condition with the absorption coefficient is defined by:

$$Q = \delta * (\alpha q - h[T - T_{amb}] - \varepsilon\sigma[T^4 - T_{amb}^4]) \quad \text{.....(7)}$$

$$q = \frac{2P}{\pi r^2}\exp\left(-2\frac{x^2}{r^2}\right) \times f(t) \quad \text{.....(8)}$$

$$f(t) = \begin{cases} 1, t \le t_p \\ 0, t > t_p \end{cases} \quad \text{.....(9)}$$

In this equation (7,8), P, r, α and δ represents the laser power, beam spot diameter, absorptivity and interface thickness respectively. q is the input heat flux, Ɛ is the emissivity and σ is the Boltzmann constant. The convective heat loss from the boundaries 1, 2, 3, 4, 5 and 6 are subjected to the equation:

$$-k\nabla T = h(T - T_{amb}) \quad \text{.....(10)}$$

At the vapor-liquid interface, the boundary condition can be defined by (Bayat et al., 2019):

$$[-p\,I + \mu(\nabla\vec{u} + (\nabla\vec{u})^T)]\vec{n} = \delta * [\sigma_s\kappa\vec{n} + \nabla_S\sigma_s] \quad \text{..(11)}$$

where, μ, σ_s and ∇_s denotes the dynamic viscosity, surface tension, and gradient operator.

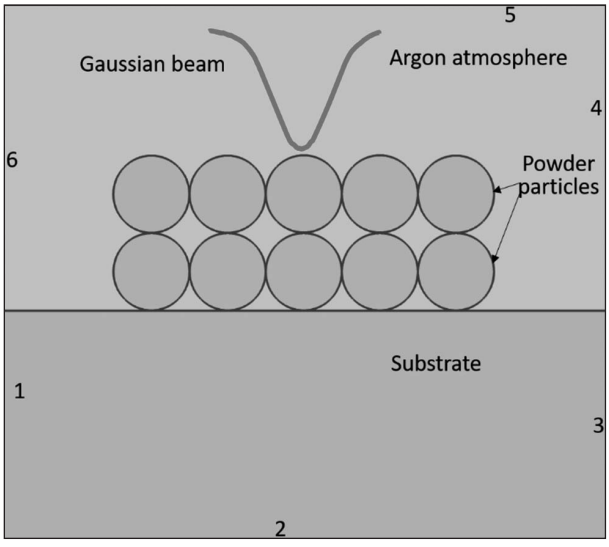

Fig. 1. Schematic diagram of computational domain with powder bed.

Table 1
Parameters used in simulation.

Name	Value
Powder bed layer thickness (L_t)	50 µm
Average size of powder particle (d)	25 µm
Laser Spot Diameter (d_{spot})	130 µm
Laser pulse width ($t_{p)}$	0.2 ms
Laser Power (P)	100 W

Table 2
Physical properties IN718 (Knapp et al., 2019; Mandal et al., 2023; Mandal et al., 2022; Sharma et al., 2019).

Properties	Symbol	Value
Solidus temperature (K)	T_s	1533
Vaporization temparature (K)	T_v	3120
Liquidus temperature (K)	T_l	1609
Density in solid (kg-m^{-3})	ρ_s	8193.3
Density in liquid (kg-m^{-3})	ρ_l	7900
Temperature dependent specific heat capacity (J-kg^{-1}-K^{-1})	C_p	460-894.8
Temperature dependent thermal conductivity (W-m^{-1}-K^{-1})	k	11.1 - 28.3
Viscosity (Pa-s)	µ	0.00531
Thermal expansion coefficient (K^{-1})	β	1.4×10^{-5}
Surface tension coefficient (N-m^{-1})	σ	1.82
Thermo-capillary coefficient (N-m^{-1}-K^{-1})	$\partial\sigma/\partial T$	-0.37 $\times 10^{-3}$
Latent heat of fusion (J-Kg^{-1})	L	2.27 $\times 10^5$
Latent heat of evaporation (J-Kg^{-1})	L_v	6.3×10^6
Absorption coefiicient	α	0.5
Atomic mass (gram)	m	58.6934
Atmosheric pressure (N-m^{-2})	P_{atm}	101300
Ideal gas constant (J-K^{-1} -mo1^{-1})	R_o	8.314
Convection coefficient (W-m^{-2}-K^{-1})	*h*	100

The mass flow rate of a vaporized particle is described by the Hertz-Langmuir relation as (Hirano et al., 2011):

$$q_v = M_v \times L_v \quad \text{.....(12)}$$

where,

$$M_v = \sqrt{\frac{m}{2\pi k_b T_s}} \times P_r(T_s) \times (1 - \beta_r)$$

where, m, k_b and L_v represent the atomic mass, Boltzmann constant and latent heat of vaporization, respectively. The Clausius-Clapeyron relation determines the vapour pressure, $P_r(T_s)$ as follows (Hirano et al., 2011):

$$P_r(T_s) = 0.54 \text{ x } P_{atm} \times exp\left(\frac{M_a L_v}{R}\left(\frac{1}{T_v} - \frac{1}{T_s}\right)\right) \quad \text{.....(13)}$$

where, M_a, R, T_v and β_r represent the molar mass, ideal gas constant, boiling temperature, and retro diffusion coefficient, respectively.

3. Material and Parameters used for Simulation

In this experiment, IN718 has been taken for both powder particles and substrate. Thermal properties and physical of IN718 alloys are shown in Table 2. The thermo-physical properties such as thermal conductivity, density, viscosity, and specific heat capacity are temperature dependent parameters. The processing parameters are listed in Table 1. The above model was used to simulate the laser micro-convex dimple using laser additive manufacturing with a pulse width of 0.2 ms. The average calculated laser beam diameter is 120 µm, with a laser power of 100 W and a pulse width of 0.2 ms. The process parameters were chosen based on the pilot experiment results and available reports. To better understand the dynamics of thermal and fluid flow in the melt pool, a numerical study has been included. It is important to note that the laser beam intensity emitted on the surface is in the order of 6.5*10^9 W/m^2. Due to very high laser beam intensity, the powder bed is melted within a few microseconds.

4. Results and Discussion

4.1. Study of temperature field

Fig. 2 demonstrate the temperature field during heating (0 ms to 0.2 ms) and cooling (0.2 ms to 1 ms).

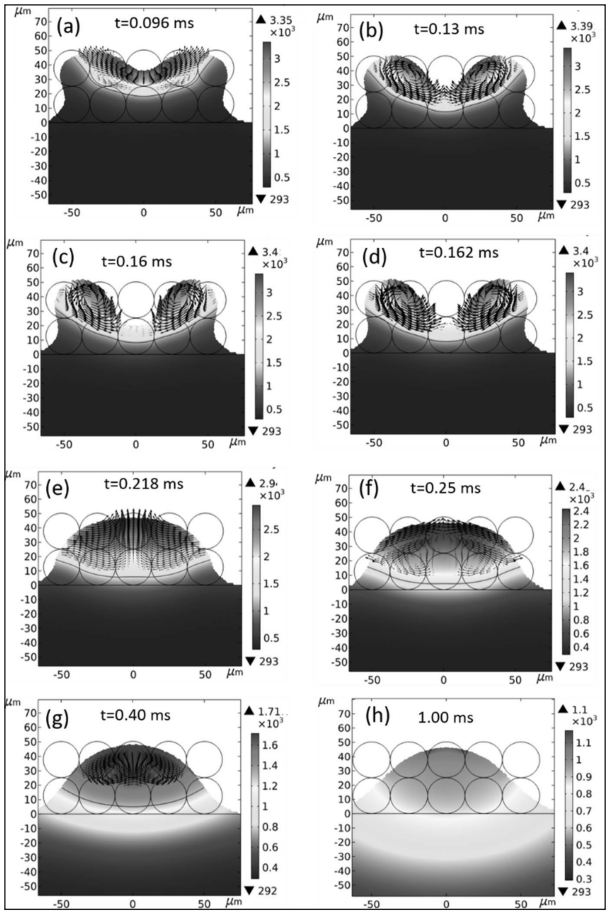

Fig. 2. Shows the temperature field distribution during heating (a-d) and cooling (e-h). Temperature is in kelvin (K).

Fig. 2(a-d) depicts the melt flow dynamics during heating at different time period such as t= 0.096, 0.13, 0.16 and 0.162 ms. Due to increase in temperature (T_{max} = 3350 K at 0.096 ms, T_{max} = ~ 3390 K at 0.13 ms, T_{max} = ~ 3400 K at 0.16 ms and T_{max} = ~ 3400 K at 0.162 ms), recoil pressure predominant at the center of the melt pool. The melt pool is depressed at the center due to recoil pressure acting in a downward direction. The depressed liquid is ~ 30 μm deep from the top surface of the powder bed (Fig. 2d).

Fig. 2(e-h), illustrate the thermo-fluidic phenomena when the laser beam is switched off. The temperature of the melt pool is ~ 2900 K which is below the vaporization temperature (~ 3120 K) at 0.218 ms. The depressed melt pool starts to flow under the influence of thermo-capillary forces, surface tension and gravitational force, respectively. From the Fig. 2(e-h), it has been observed that with decrease in the melt pool temperature, the depressed liquid to grew approximately ~ 26 μm, which is ~ 4 μm less than the actual layer thickness in the computational domain.

4.2. Experimental validation

Fig. 3(a-d) represent the 3D optical profilometry images from 1st to 4th pulses. The obtained width and height of the dimples from the optical profilometry data are shown in Fig. 3. (e-h). The optical profilometry images show that as the

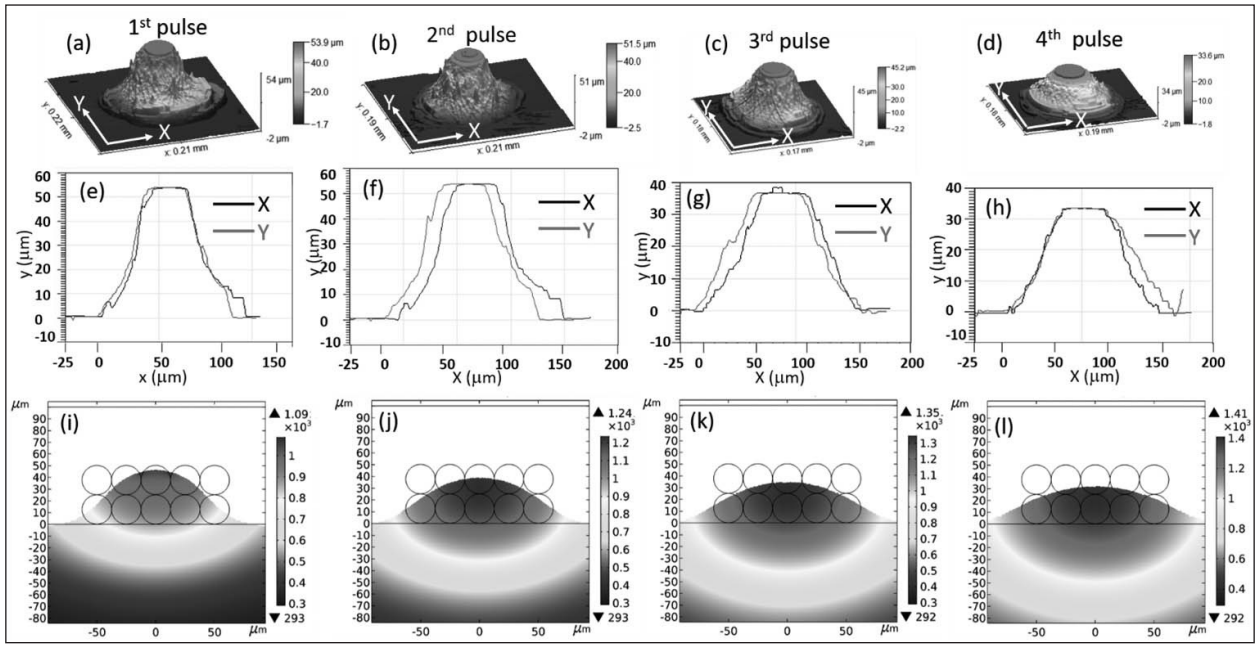

Fig. 3. (a-d) Illustrates optical profilometry images, (e-h) represent the 2D surface profile from optical profilometry data in X and Y axes, and (i-l) shows the numerical results after solidifications.

number of pulses increases, the height of the micro-convex dimple increases. A numerical simulation has been developed to validate the experimental results of the geometrical dimension of the micro-convex dimple.

Fig. 3(i-l), represents the numerical results after solidification for 1st, to 4th pulses respectively. The average height of experimental (i.e., optical profilometry result) and simulated results from the first to fourth pulses has been calculated. The above results show that the numerical results are very similar to the experimental results. The maximum and minimum height differences between experimental and numerical results are ~ 12.5 μm and ~ 1.6 μm, respectively. However, the maximum and minimum width differences of the micro-convex dimple are ~ 27 μm and ~ 20 μm, respectively. According to the findings of the preceding study, the experimental results are in good agreement with the numerical results.

5. Conclusions

In this study, a 2D finite element model (FEM) was produced to understand the thermo-fluidic behavior of the melt pool, and experiments were performed to understand the surface characteristics in the micro-convex dimple. Based on this model, after reaching the vaporization temperature of IN718 (~ 3120 K) in the melt pool, recoil pressure dominates, resulting in a depression in the melt pool. When the laser is turned off, the temperature in the melt pool begins to fall. As the temperature in the melt pool falls below the vaporization temperature, the depressed melt pool begins to rise due to the influence of thermo-capillary forces. The maximum and minimum differences in the melt pool height between experimental and numerical values are ~ 12.5 μm and ~ 1.6 μm, and the melt pool width are ~ 27 μm and ~ 20 μm, respectively.

References

Bayat, M., Thanki, A., Mohanty, S., Witvrouw, A., Yang, S., Thorborg, J., Tiedje, N. S., & Hattel, J. H. (2019). Keyhole-induced porosities in Laser-based powder bed fusion (L-PBF) of Ti6Al4V: High-fidelity modelling and experimental validation. *Additive Manufacturing*, *30*(July), 100835. https://doi.org/10.1016/j.addma.2019.100835

Dinda, G. P., Dasgupta, A. K., & Mazumder, J. (2012). Texture control during laser deposition of nickel-based superalloy. *Scripta Materialia*, *67*(5), 503-506.

Etsion, I. (2005). State of the art in laser surface texturing. *Journal of Tribology*, *127*(1), 248-253.

Gan, Z., Yu, G., He, X., & Li, S. (2017). Numerical simulation of thermal behavior and multicomponent mass transfer in direct laser deposition of Co-base alloy on steel. *International Journal of Heat and Mass Transfer*, *104*, 28-38.

Hirano, K., Fabbro, R., & Muller, M. (2011). Experimental determination of temperature threshold for melt surface deformation during laser interaction on iron at atmospheric pressure. *Journal of Physics D: Applied Physics*, *44*(43).https://doi.org/10.1088/0022-3727/44/43/435402

Jiao, L., Chua, Z. Y., Moon, S. K., Song, J., Bi, G., & Zheng, H. (2018). Femtosecond laser produced hydrophobic hierarchical structures on additive manufacturing parts. *Nanomaterials*, *8*(8), 601.

Knapp, G. L., Raghavan, N., Plotkowski, A., & Debroy, T. (2019). Experiments and simulations on solidification microstructure for Inconel 718 in powder bed fusion electron beam additive manufacturing. *Additive Manufacturing*, *25*, 511-521.

Mandal, V., Sharma, S., Singh, S. S., & Ramkumar, J. (2022). Laser surface texturing in powder bed fusion: numerical simulation and experimental characterization. *Metals and Materials International*, *28*(1), 181-196.

Mandal, V., Tripathi, P., Kumar, A., Singh, S. S., & Ramkumar, J. (2022). A study on selective laser melting (SLM) of TiC and B4C reinforced IN718 metal matrix composites (MMCs). *Journal of Alloys and Compounds*, *901*, 163527.

Mandal, V., Tripathi, P., Sharma, S., Jayabalan, B., Mukherjee, S., Singh, S. S., & Ramkumar, J. (2023). Fabrication of ex-situ TiN reinforced IN718 composites using laser powder bed fusion (L-PBF): Experimental characterization and high-fidelity numerical simulations. *Ceramics International*.

Otero, N., Romero, P., Gonzalez, A., & Scano, A. (2012). Surface texturing with laser micro cladding to improve tribological properties. *Journal of Laser Micro/Nanoengineering*, *7*(2).

Romero, P., Otero, N., González, A., García, G., & Scano, A. (2011). Additive generation of surface microstructures for fluid-dynamic applications by using single-mode fibre laser assisted microcladding. *Physics Procedia*, *12*, 268-277.

Sarker, A., Tran, N., Rifai, A., Elambasseril, J., Brandt, M., Williams, R., Leary, M., & Fox, K. (2018). Angle defines attachment: Switching the biological response to titanium interfaces by modifying the inclination angle during selective laser melting. *Materials & Design*, *154*, 326-339.

Sharma, S., Mandal, V., Ramakrishna, S. A., & Ramkumar, J. (2019). Numerical simulation of melt pool oscillations and protuberance in pulsed laser micro melting of SS304 for surface texturing applications. *Journal of Manufacturing Processes*, *39*, 282-294.

Simonelli, M., Tse, Y. Y., & Tuck, C. (2014). On the texture formation of selective laser melted Ti-6Al-4V. *Metallurgical and Materials Transactions A*, *45*(6), 2863-2872.

Wang, M., Wu, Y., Lu, S., Chen, T., Zhao, Y., Chen, H., & Tang, Z. (2016). Fabrication and characterization of selective laser melting printed Ti–6Al–4V alloys subjected to heat treatment for customized implants design. *Progress in Natural Science: Materials International*, *26*(6), 671-677.

Wei, H. L., Mazumder, J., & DebRoy, T. (2015). Evolution of solidification texture during additive manufacturing. *Scientific Reports*, *5*(1), 1-7.

Zhou, X., Li, K., Zhang, D., Liu, X., Ma, J., Liu, W., & Shen, Z. (2015). Textures formed in a CoCrMo alloy by selective laser melting. *Journal of Alloys and Compounds*, *631*, 153-164.

Dr. Vijay Mandal is a Post Doctoral Fellow in the department of Metallurgical and Materials Science at Indian Institute of Technology Bombay. He obtained his Ph.D in Mechanical Engineering from IIT Kanpur in 2022. His research focuses on the laser powder bed fusion (L-PBF) additive manufacturing process.

Vikas Tiwari is a Research Scholar in the Department of Materials Science and Engineering at Indian Institute of Technology Kanpur. He obtained his B.Tech degree from Maulana Azad National Institute of Technolog Bhopal.
(E-mail: vikast20@iitk.ac.in)

Moloy Sarkar is a Research Scholar in the Department of Mechanical Engineering at Indian Institute of Technology Kanpur. He obtained his B.Tech degree from Jalpaiguri Government Engineering College, West Bengal.
(E-mail: moloys21@iitk.ac.in)

Dr. Sudhanshu Shekhar Singh is an Associate Professor in the Department of Materials Science and Engineering at Indian Institute of Technology Kanpur. He obtained his Ph.D degree from Arizona State University. He is a recipient of NASI-Young Scientist Platinum Jubilee Awards 2020 by The National Academy of Sciences (India), 2018SMD JOM Best Paper Award by The Minerals, Metals & Materials Society (TMS), Young Metallurgist of the Year Award 2017 by Ministry of Steel & Mines (India) and IEI Young Engineers Award 2017–2018 by The Institution of Engineers (India). (E-mail: sudhanss@iitk.ac.in)

Dr. J. Ramkumar, Professor in the Department of Mechanical Engineering and Design Program at Indian Institute of Technology Kanpur, has over 20 years of experience in industry, research and academia. He obtained his Ph.D in Mechanical Engineering from Indian Institute of Technology Madras. He joined as an Assistant Professor in the Department of Mechanical Engineering in Dec 2003. He has published over 330 articles in the peer-reviewed international journals and has delivered over 100 lectures in the international conferences. He has 4000+ citations for his publications & his h-index of 33, which endorses his high research productivity. Five of his patents are commercialized, total number of patents in his name being 88. Currently, he is the Project Investigator of MedTech facility, Imagineering Laboratory and RuTAG facility at IIT Kanpur. (E-mail: jrkumar@iitk.ac.in)